5. M.J. Lazarus and S. Petithomme, The Fresnel rhomb as a millimetre-wave circular polarizer, Microwave Opt Technol Lett 20 (1999), 353–357.
6. R.S. Longhurst, Geometrical and physical optics, Longmans, London, 1976, p. 20.
7. M.J. Lazarus, Optical bulb lens-antenna for efficient plastic fibre coupling, Microwave Opt Technol Lett 28 (2001), 141–143.

A STUDY OF MICROWAVE THERMAL EMISSION FROM A SUBSURFACE OBJECT

Baran U. Ungan and Joel T. Johnson
Department of Electrical Engineering and ElectroScience Laboratory
The Ohio State University
205 Dreese Laboratories
2015 Neil Ave
Columbus, Ohio 43210

Received 8 October 2001

ABSTRACT: *A numerical study of microwave thermal emission from a finite-size buried object is described. Results show that emission from a finite-size object can exhibit properties similar to emission from a layered (i.e., horizontally infinite) model of the object, including an oscillatory behavior versus frequency.* © 2002 Wiley Periodicals, Inc.
Microwave Opt Technol Lett 33: 9–12, 2002; DOI 10.1002/mop.10214

Key words: *mine detection; microwave radiometry; thermal emission; ground penetrating radar*

1. INTRODUCTION

Microwave radiometers have been shown to be effective sensors for monitoring soil moisture and other geophysical data [1, 2]. Models for geophysical-medium brightness temperatures often consider horizontally stratified geometries, because exact evaluation of observed brightness temperatures is possible for this case in terms of a sum involving layered-medium reflection quantities [3]. For cases involving media at uniform physical temperature, the formulation reduces to Kirchhoff's law which relates emissivity to one minus the reflection coefficient of the layered medium.

Recent studies have begun to consider the use of microwave radiometers for detecting shallow, subsurface objects such as antipersonnel landmines [4, 5]. Modeling studies [5] based on Kirchhoff's law and the three-layer, horizontally stratified geometry shown in Figure 1(a) (i.e., objects are infinite layers) show that significant brightness-temperature contrasts can be obtained in the presence of a subsurface object if sufficient dielectric contrast is available and if soil-medium attenuation is not excessive. Reference [5] further demonstrated that use of multifrequency brightness measurements could potentially provide detection of objects even with low contrast or high attenuation due to the oscillatory behavior versus frequency observed in the presence of an object. Estimated environmental effects such as local surface temperature or soil moisture variations would not produce oscillatory frequency behavior (except in unusual circumstances [2]), so that detections would still be possible even in the presence of environmental clutter. The possibility of directly detecting the dielectric contrast of a subsurface object suggests an advantage for microwave passive sensors as compared to passive infrared [6] or millimeter-wave sensors in which only surface-temperature effects are detected.

Contract grant sponsors: NSF Project No. ECS-9701678; Duke University.

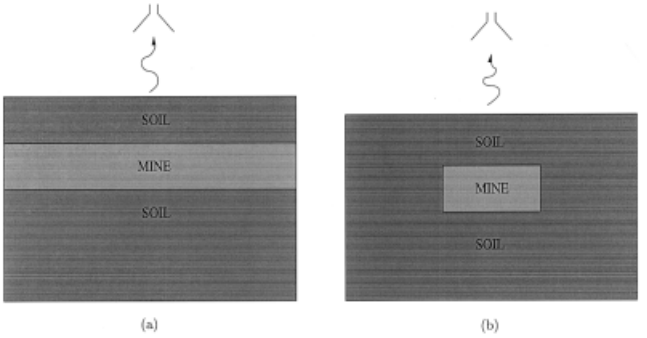

Figure 1 (a) Layered-medium model for a subsurface object. (b) A finite-size subsurface object

However, previous buried-object detection models have neglected effects of finite object size [Figure 1(b)], because subsurface objects were modeled as horizontally infinite layers. Numerically calculated emission results from a finite-size buried object are considered in this Letter, through use of a numerical solution of the electromagnetic boundary value problem. The model applied is based on an iterative method of moments (including half-space Sommerfeld Green's functions) accelerated with the discrete dipole approximation [7–10]. Brightness temperatures and their variations with frequency are presented for a sample case, and amplitudes of brightness-temperature oscillations in frequency are shown to vary according to the fraction of the observing antenna pattern occupied by the subsurface object. Finite-size object solutions are also compared with results from the horizontally infinite layer model to determine the parameter space under which the layered model is applicable.

2. FORMULATION

A constant temperature medium is assumed so that brightness temperatures can be calculated with the use of Kirchhoff's law:

$$T_B = T_s(1 - R), \tag{1}$$

where T_B is the brightness temperature measured by an observing radiometer, T_s is the physical temperature of the medium and subsurface object (taken as 290 K in this Letter), and R is the total reflectivity of the medium. The brightness temperature T_B is a function of the radiometer polar and azimuthal observation angles θ and ϕ (respectively), the frequency of observation f, the polarization of the radiometer, the dielectric properties of the medium in which the object is buried, and the geometric and dielectric properties of the subsurface object. The total reflectivity R is equal to the total power scattered into the free-space region when the subsurface object is illuminated by a plane-wave field incident from angles θ and ϕ in the free-space region with a polarization identical to that of the radiometer, and can therefore be determined by solving the corresponding scattering problem [3].

For an object modeled as an infinite layer, fields in the free-space region consist only of the incident and reflected plane waves, with R determined by the amplitude of the reflected plane wave. However, in the presence of a finite-size object, total fields in the free-space region include both incident and reflected plane waves and spherical scattered wave components. The brightness temperature is then expressed as

$$T_B = T_s\left(1 - |\Gamma|^2 - \frac{P_{c0} + P_{s0}}{P_i}\right), \tag{2}$$

where Γ is the plane-wave reflection coefficient of the half-space boundary, P_{s0} is the total scattered spherical wave power above the interface due to the subsurface object, and P_{c0} is a cross-power term due to the interaction of the reflected plane wave and scattered spherical waves. Both these terms are normalized by the total power incident on the half-space medium P_i. The above equation is most conveniently derived by initially considering a tapered incident field [11] and evaluating the brightness temperature in the limit of a very large spot size on the boundary (i.e., the plane-wave limit).

If the half-space medium and object are assumed to be lossless, the same brightness temperature can also be calculated with the use of the power radiated into the half-space medium as

$$T_B = T_s\left(|T|^2 \frac{\eta_0}{\eta_1} + \frac{P_{c1} + P_{s1}}{P_i}\right), \tag{3}$$

where T represents the plane-wave transmission coefficient at the boundary, η_0 and η_1 are the characteristic impedances of free space and the half-space medium, respectively, and P_{s1} and P_{c1} are the scattered power and the cross-power terms, respectively, in the half-space medium. Comparison of the brightness temperatures obtained from Eqs. (2) and (3) provides information on the level of power conservation obtained in the numerical solution; results will be plotted for brightnesses obtained from both methods.

For a plane-wave incident field, the cross-power terms can be shown to reduce to

$$P_{c0} = \frac{2\pi}{\omega\mu} \operatorname{Im}\{\hat{e}_r \cdot \bar{F}_s \Gamma\} \tag{4}$$

and

$$P_{c1} = \frac{2\pi}{\omega\mu} \operatorname{Im}\{\hat{e}_t \cdot \bar{F}_s T\}, \tag{5}$$

where $\omega = 2\pi f$ is the radian frequency of the radiometer, μ is the permeability of free space, Im denotes the imaginary part operator, $\hat{e}_r$ and $\hat{e}_t$ are unit vectors in the directions of the half-space reflected and the transmitted plane wave electric fields, respectively, and $\bar{F}_s$ is the scattered spherical-wave amplitude in the reflected (for P_{c0}) or transmitted directions (for P_{c1}). The above equations are equivalent to an optical theorem [3] for an object in a lossless half-space.

Spherical-wave scattered fields from a subsurface object under plane-wave illumination were numerically evaluated with the use of an iterative method-of-moments algorithm. Because a half-space (Sommerfeld) Green's function was employed in the formulation, discretization was required only on the subsurface object, which was sampled onto a three-dimensional uniform Cartesian grid. Use of the volume equivalence principle and a point-matching approach reduces the integral equations of the method of moments to a matrix equation for coupling between a set of discrete dipoles [7]. Computational efficiency is improved through the methods described in [8–10], so that electromagnetic coupling between all points on the object grid is computed in order $N \log N$, where N is the number of sampling points. In the brightness-temperature calculations the cross-power term is computed with the use of only specular scattered fields, whereas the scattered spherical-wave power term requires a numerical integration of far-zone scattered powers over the upper or lower hemispheres. Tests varying the number of points in this integration were performed to ensure accurate total scattered power computations.

To clarify the influence of a subsurface object, results will be presented in terms of the brightness temperature change caused by the presence of the object. Because the scattered power and cross-power terms vanish when no object is present, the change in the brightness temperatures caused by the object is

$$\Delta T_B = -T_s\left(\frac{P_{c0} + P_{s0}}{P_i}\right) = T_s\left(\frac{P_{c1} + P_{s1}}{P_i}\right). \tag{6}$$

A final issue involves evaluation of the P_i term when plane wave observations are considered. Because a plane wave would illuminate an infinite portion of the half-space in the corresponding scattering problem, P_i approaches infinity and the effect of the object becomes negligible. In fact, a radiometer observing a subsurface object would be sensitive to only a finite-sized portion of the half-space, so that P_i remains finite and approximately equal to

$$P_i \approx \frac{1}{2\eta_0} A \tag{7}$$

for nadiral observations ($\theta = 0$). Here A is the spot-size area of the observing antenna, which is assumed to have dimensions comparable to or larger than the electromagnetic wavelength so that the plane-wave field model used in the numerical solution is valid. To make the results presented independent of the antenna spot size A, brightness temperature deviations are rewritten as

$$\Delta T_B = -T_s\left(\frac{P_{c0} + P_{s0}}{\dfrac{1}{2\eta_0} A_{\text{obj}}}\right)\left(\frac{A_{\text{obj}}}{A}\right) \tag{8}$$

$$= -T_s\left(\frac{P_{c0} + P_{s0}}{\dfrac{1}{2\eta_0} A_{\text{obj}}}\right) F, \tag{9}$$

where A_{obj} is the cross-sectional area of the object. The term F in the final equation thus represents a beam fill factor that describes the fraction of the observing antenna pattern occupied by the subsurface object. The following plots use $F = 1$ for simplicity; it should be noted that the curves presented are to be multiplied by F for a specified antenna and object in order to predict the brightness changes observed by that antenna.

3. RESULTS

Figure 2 illustrates ΔT_B as a function of frequency from the numerical solution (symbols) for a half-space relative permittivity of 4 and object relative permittivity of 3.15 (close to the values for dry soil and plastic, respectively.) The object is a cube with side length 2 cm centered 5 cm below the boundary, and was discretized into 16 by 16 by 16 points to ensure accurate calculations over this range of frequencies. Nadiral observation $\theta = 0$ is considered, and the radiometer polarization is aligned with the cube edge. Numerical ΔT_B values plotted from both the reflected and the transmitted powers are in agreement to within approximately 2 K, confirming power conservation in the numerical solution to better than 1%. Results from the layered medium model (i.e., with the object modeled as an infinite layer) are also included as the solid curve in Figure 2, and show good agreement with finite-size object brightness deviations even though the object is

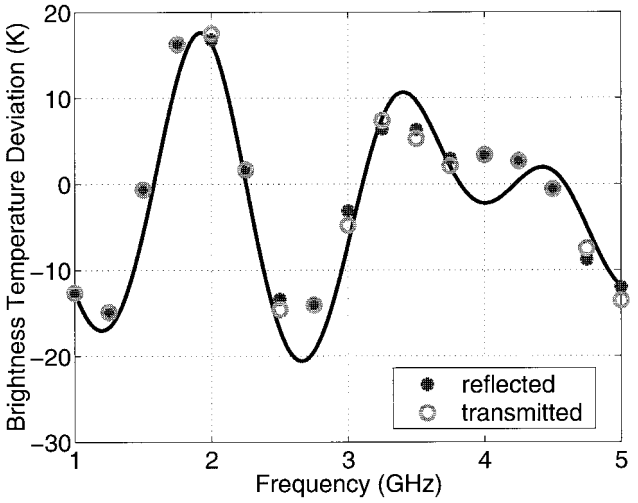

Figure 2 Brightness temperature deviation versus frequency—numerical solution (discrete points) compared with layered model (solid curve)

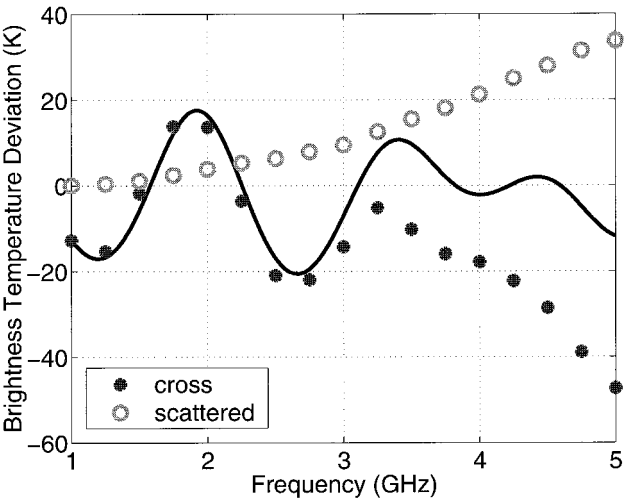

Figure 4 Contributions of scattered and cross-power terms to brightness temperature deviations with the use of the fields below the ground. Numerical solution (discrete points) compared with total brightness deviation from layered model (solid curve)

relatively small compared to the wavelengths considered. Only slight effects due to finite object size are observed, primarily at the higher frequencies, although again the beam fill factor for a specific antenna would reduce finite-object results proportionately. Overall, results show that finite-size object effects are not likely to modify the basic strategy of searching for oscillatory brightness features for detecting objects.

Figures 3 and 4 illustrate the individual contributions of the scattered spherical-wave power and the cross-power terms to the ΔT_B results of Figure 2. The brightness temperature difference computed with the use of the fields above the interface is presented in Figure 3. For this case the scattered power term is generally negligible as compared to the cross-power term. Unlike the case for the fields above the interface, the scattered-power and the cross-power terms both show important contributions with fields below the interface, as shown in Figure 4. However, the two power terms still add up to give an accurate ΔT_B. This increase in the scattered power below the ground is possibly due to the fact that the object size is larger as compared to the wavelength in the medium.

Brightness temperature results for the slightly tilted object shown in Figure 5 are presented in Figure 6. Because the tilted object is represented on the original (untilted) grid, discretization error in the object boundary can potentially be significant. However, several tests of the results were performed to ensure that the results presented are accurate to within 2 K. Results show that only moderate changes in brightness temperatures are observed as the object is tilted to an angle of $\alpha = 20°$.

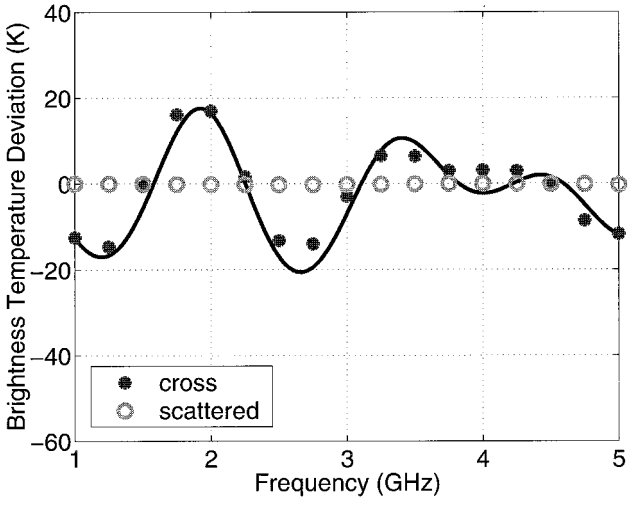

Figure 3 Contributions of scattered and cross-power terms to brightness-temperature deviations with the use of the fields above the ground. Numerical solution (discrete points) compared with total brightness deviation from layered model (solid curve)

4. CONCLUSIONS

Effects of finite object size on the detection of buried objects using microwave radiometry have been investigated. Thermal emission from buried objects has been shown to display an oscillatory behavior versus frequency, providing a means for detecting objects. Although finite-size object effects do affect the specific brightness temperature of the buried object, the basic strategy of searching for oscillatory features versus frequency for object detection appears to remain valid.

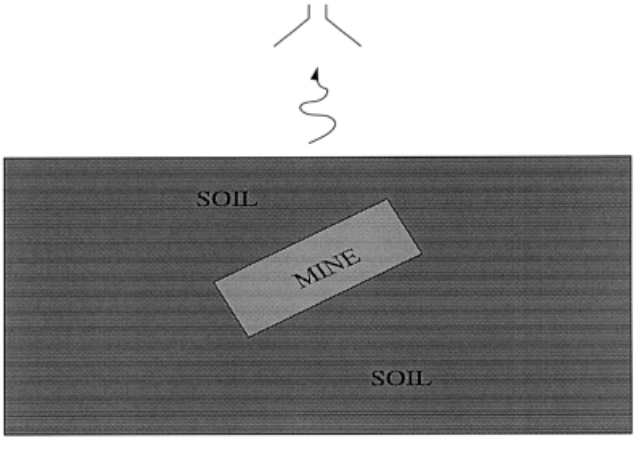

Figure 5 Geometry of tilted subsurface object

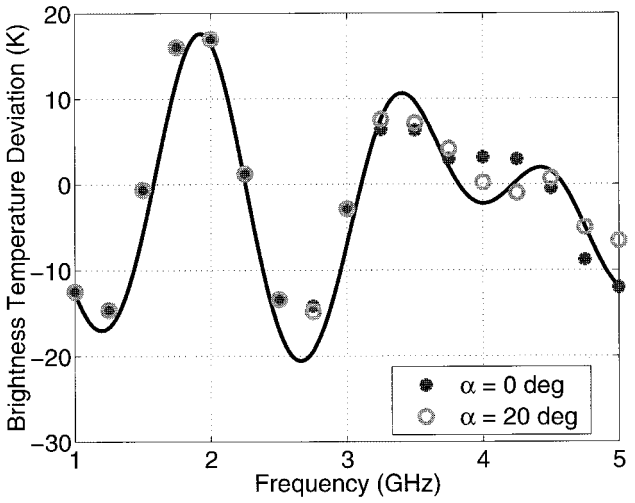

Figure 6 Comparison of brightness temperatures for tilted and untilted objects with layered-medium model

REFERENCES

1. F.T. Ulaby, R.K. Moore, and A.K. Fung, Microwave remote sensing: active and passive, Artech House, Norwood, MA, 1986.
2. T.J. Schmugge, T.J. Jackson, P.E. O'Neill, and M.B. Parlange, Observations of coherent emissions from soils, Radio Sci 33 (1998), 267–272.
3. L. Tsang, J.A. Kong, and R.T. Shin, Theory of microwave remote sensing, Wiley, New York, 1985.
4. G. De Amici, B. Hauss, and L. Yujiri, Detection of landmines via a passive microwave radiometer, Proc SPIE 3710 (1999), 716–724.
5. J.T. Johnson, Theoretical study of microwave radiometry for buried object detection, Proc SPIE 4038 (2000), 286–297.
6. I.K. Sendur and B.A. Baertlein, Techniques for improving buried mine detection in thermal IR imagery, Proc SPIE 3710 (1999), 1272–1283.
7. B.T. Draine and P.J. Flatau, Discrete-dipole approximation for scattering calculations, J Opt Soc Am A 11 (1994), 1491–1499.
8. P.J. Flatau, Improvements in the discrete-dipole approximation method of computing scattering and absorption, Opt Lett 22 (1997), 1205–1207.
9. T.J. Cui and W.C. Chew, Fast algorithm for electromagnetic scattering by buried 3-D objects of large size, IEEE Trans Geosci Remote Sensing GRS-37 (1999), 2597–2608.
10. J.T. Johnson and R.J. Burkholder, Coupled canonical grid/discrete dipole approach for computing scattering from objects above or below a rough interface, IEEE Trans Geosci Remote Sensing GRS-39 (2001), 1214–1220.
11. H. Braunisch, Y. Zhang, C.O. Ao, S.E. Shih, Y.E. Yang, K.H. Ding, J.A. Kong, and L. Tsang, Tapered wave with dominant polarization state for all angles of incidence, IEEE Trans Antennas Propaget AP-48 (2000), 1086–1095.

TILT ANGLE AND SIDE-LOBE LEVEL CONTROL OF MICROWAVE ARRAY ANTENNAS

Vilson Rodrigo Mognon, Wilson Arnaldo Artuzi Jr., and Jose Ricardo Descardeci
Dep. Eng. Eletrica
Universidade Federal do Parana–UFPR
Centro Politecnico
CP 19011
81531-990 Curitiba PR, Brazil

Received 10 October 2001

ABSTRACT: *This article describes a new strategy for controlling the tilt angle and side-lobe level of linear array antennas by using a genetic algorithm. A very simple fitness function for controlling the performance of the array was constructed and is suggested. Simulations show excellent results for directing the main lobe and side-lobe levels.* © 2002 Wiley Periodicals, Inc. Microwave Opt Technol Lett 33: 12–14, 2002; DOI 10.1002/mop.10215

Key words: *array antennas; microwave antennas; genetic algorithm*

I. INTRODUCTION

Periodic arrays are largely employed in communication systems. Array antennas can be easily implemented and present the flexibility to control the direction of radiation, gain, side-lobe levels, et cetera [1]. These periodic arrays generate a low side-lobe amplitude taper by strategically positioning equally weighted elements. Simple analytical methods for deriving the element positions to obtain a desired side-lobe level are not available [2]. Probabilistic methods can also be applied for controlling relative side-lobe level (RSLL), but these are not accurate enough [3]. Haupt [4] presented a means of thinning an array by turning off some elements in a periodic array in order to improve RSLL. The method presented in [4] uses the genetic-algorithm technique and normally arrives at optimized thinning configurations for large arrays, where other methods cannot be applied [5].

The aim of this article is to present an exercise of optimization of array antennas by using the genetic-algorithm technique, considering a simple and practical developed fitness function. Initially, it is considered a set of parameters that carries all the information to be optimized. This set of parameters is called the chromosome, and it is evaluated by the fitness function. The chromosome will contain the information about the uniform phase variation along the array, and also the amplitude excitation level of each array element as input parameters. The fitness function will take into account the desired direction of the main lobe and the RSLL. In this work, two examples considering a linear array of 40 elements are presented. In the first example, results have shown a very low side-lobe level of -32.9 dB with the use of a $\lambda/10$-element spacing (this value is 12.9 dB below that reported in the literature [5] with an identical linear array antenna). In the second example a more practical spacing of 0.3λ separates the elements, and simulation still shows a very good result of -28 dB of RSLL.

II. THEORY

Genetic-algorithm optimizers are robust stochastic search methods, modeled on the principles and concepts of natural selection and evolution [5]. The algorithm begins by initializing a popula-

Correspondence to: Jose Ricardo Descardeci, Dep. Eng. Eletrica, Universidade Federal do Parana–UFPR, Centro Politecnico, CP 19011, 81531-990 Curitiba PR, Brazil (descar@eletrica.ufpr.br)
Contract grant sponsors: Brazilian agencies CNPq and FUNPAR